

## Three-dimensional Magnetic and Thermodynamic Structures of Solar Microflares

Z. F. LI,<sup>1,2</sup> X. CHENG,<sup>1,3,2</sup> F. CHEN,<sup>1,2</sup> J. CHEN,<sup>1,2</sup> AND M. D. DING<sup>1,2</sup>

<sup>1</sup>*School of Astronomy and Space Science, Nanjing University, Nanjing, 210046, People's Republic of China*

<sup>2</sup>*Key Laboratory of Modern Astronomy and Astrophysics (Nanjing University), Ministry of Education, Nanjing 210093, China*

<sup>3</sup>*Max Planck Institute for Solar System Research, Gottingen, D-37077, Germany*

(Received ...; Revised ...; Accepted ...)

Submitted to ApJL

### ABSTRACT

Microflares, one of small-scale solar activities, are believed to be caused by magnetic reconnection. Nevertheless, their three-dimensional (3D) magnetic structures, thermodynamic structures, and physical links to the reconnection have been unclear. In this Letter, based on high-resolution 3D radiative magnetohydrodynamic simulation of the quiet Sun spanning from the upper convection zone to the corona, we investigate 3D magnetic and thermodynamic structures of three homologous microflares. It is found that they originate from localized hot plasma embedded in the chromospheric environment at the height of 2–10 Mm above the photosphere and last for 3–10 minutes with released magnetic energy in the range of  $10^{27} - 10^{28}$  erg. The heated plasma is almost co-spatial with the regions where the heating rate per particle is maximal. The 3D velocity field reveals a pair of converging flows with velocities of tens of  $\text{km s}^{-1}$  toward and outflows with velocities of about  $100 \text{ km s}^{-1}$  moving away from the hot plasma. These features support that magnetic reconnection plays a critical role in heating the localized chromospheric plasma to coronal temperature, giving rise to observed microflares. The magnetic topology analysis further discloses that the reconnection region is located near quasi-separators where both current density and squashing factors are maximal although the specific topology may vary from tether-cutting to fan-spine-like structure.

*Keywords:* Solar flares (1496); Solar magnetic reconnection(1504); Solar coronal heating (1989)

### 1. INTRODUCTION

Solar flares refer to rapid enhancements of electromagnetic emissions in the solar atmosphere and generally originate from strong magnetic field concentrated active regions. In the standard flare model, i.e., so-called CSHKP model (Carmichael 1964; Sturrock 1966; Hirayama 1974; Kopp &

Pneuman 1976), magnetic reconnection is believed to play a substantial role in quickly releasing prestored magnetic energy to heat the plasma. In addition, solar flares are also accompanied with coronal mass ejections (CMEs) (e.g., Zhang et al. 2001; Cheng et al. 2020) and their association rate usually increases with the magnitude of flares (Yashiro et al. 2005). The rate even reaches 100% for flares with a peak of soft X-ray (SXR) 1–8 Å flux larger than  $3 \times 10^{-4} \text{ W m}^{-2}$ .

Differing from energetic flares, microflares are small-scale and short-lived solar activities. They are frequently observed in the regions where the magnetic field is diffuser and weaker than that of active regions (e.g., Kuhar et al. 2018). The energy distribution from microflares to major flares is well known to obey a power-law form (Figure 14 of Aschwanden & Parnell (2002)). Although the released energy during once microflare is small, the number is much larger than that of major flares. This means that the total energy deposited into the corona by these small-scale flares is even higher than that by large-scale flares, even may be responsible for corona heating (Hudson 1991). Microflares are also found to be closely associated with other small-scale activities such as UV bursts (Peter et al. 2014), coronal bright points (CBPs, Zhang et al. 2001), and hot loops in moss regions (e.g., Graham et al. 2019; Testa et al. 2020). These phenomena can be best discriminated and studied by extreme-ultraviolet (EUV) imaging and spectroscopic data. Various observational properties including their morphologies, evolution of magnetic field, and temperature structures suggest that microflares are produced by magnetic reconnection (e.g., Qiu et al. 2004; Ning 2008; Jess et al. 2010; Glesener et al. 2017), which is also verified by some numerical simulations (e.g., Jiang et al. 2010; Jiang et al. 2012; Archontis & Hansteen 2014).

Very recently, the Extreme Ultraviolet Imager (EUI; Rochus et al. 2020) on board Solar Orbiter (SO; Müller et al. 2020) performed observations of the quiescent corona in the 174 Å passband near the disk center, which is dominated by Fe IX and Fe X emissions at 1 MK. The unprecedented high-resolution data collected by High Resolution Imagers (HRIs) of the EUI make it possible to resolve microflares, which was difficult for previous instruments. Figure 1a shows one snapshot of the EUI 174 Å passband on 2020 May 20 when the Solar Orbiter was located at 0.612 AU away from the Sun. At this moment, the pixel size is approximately 217 km. Figure 1b and 1c display the same field of view but at the 131 Å and 171 Å passbands of the Atmospheric Imaging Assembly (AIA; Lemen et al. 2012) on board Solar Dynamical Observatory. One can clearly see microflares at different scales at the three EUV passbands but with a higher clarity for the EUI than for the AIA (Chitta et al. 2021; Chen et al. 2021b). Besides, the Spectrometer/Telescope for Imaging X-rays (STIX; Krucker et al. 2020) on board SO also observed many microflares (e.g., Saqri et al. 2022).

Nevertheless, only relying on multiwavelength imaging and spectroscopic data, the 3D magnetic and thermodynamic structures behind microflares are still difficult to be determined. To address this question, in this Letter, we mainly focus on high-resolution simulation data with a grid size of 192 km, which is comparable with the spatial resolution of the EUI/HRI on 2020 May 20. In Section 2, we give a brief description of 3D radiative magnetohydrodynamic simulation data we used. Section 3 presents the main results, including 3D magnetic and thermodynamic structures of microflares. Summary and discussion are given in Section 4.

## 2. NUMERICAL SIMULATION DATA

The numerical simulation is conducted with the MURaM radiative MHD code (Vögler et al. 2005; Rempel 2017) that solves fully compressible MHD equations with radiative transfer for optically thick radiation, optically thin radiative loss, and anisotropic thermal conduction. The computational



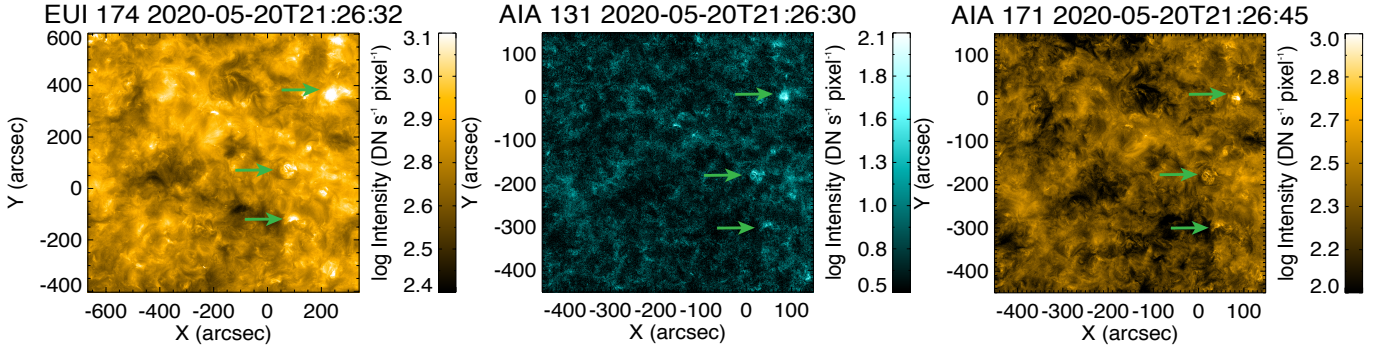


**Figure 1.** EUV images showing three microflares observed on 2020 May 20. The left panel is the EUI/HRI 174 Å image. The middle and right panels display the AIA 131 Å and 171 Å images, respectively. The locations of the three microflares are indicated by three arrows in green.

domain covers an area of  $197^2 \text{ Mm}^2$  in the horizontal directions. The vertical extent is 131 Mm with the bottom boundary placed at 18 Mm beneath the photosphere. The domain is resolved by  $1024 \times 1024 \times 2048$  grid points, corresponding to spatial resolutions of 192 and 64 km in the horizontal and vertical directions, respectively. This simulation is the “QS run” in a comprehensive simulation of magnetic flux emergence from the convection zone to the corona (Chen et al. 2021a). More details on the simulation setup and general properties of the coronal plasma and magnetic field are presented in the reference. In brief, the magnetic field in the quiet Sun is a small-scale mixed polarity field maintained by a small-scale dynamo in the convective layers of the domain. The surface magnetoconvection provides an upward Poynting flux that is dissipated in the corona. A hot corona of about 1 MK is self-consistently maintained for 11.5 hours evolution of the simulation.

### 3. RESULTS

#### 3.1. Overview of Microflares

Taking advantage of the simulated temperature and emission measure, we calculate the total soft X-ray (SXR) 1–8 Å flux and synthesize the AIA EUV images with the AIA response functions **using the `ai_get_response.pro` procedure, available in the SolarSoft Ware (SSW, Freeland & Handy 1998)**. Figure 2a shows the synthesized AIA 131 Å and 171 Å images at the three selected times (near the peak times), from which one can see that the simulated microflares present more details than observations. Moreover, the SXR 1–8 Å flux shows that there seems to occur three microflares in succession during the time period of about half an hour with the first one being much longer-lasting than the latter two (Figure 2b; also see the online animation).

The three homologous microflares originate from a small region of  $29 \times 23 \text{ Mm}^2$ , and are all visible at six synthetic AIA EUV passbands. For each event, its structure is complex and composed of many interlaced loops as shown in Figure 2a. Because of the similarity of the morphology at different passbands, we here only display the AIA 131 Å and 171 Å images. The visibility of the microflares at all AIA EUV passbands indicates that they are multithermal as suggested by previous observations (Inglis & Christe 2014). **This property is also confirmed by the differential emission measure (DEM) of the brightenings which distributes in a wide temperature range.** Moreover, the coronal emissions of the three microflares are found to significantly vary with time, indicating a time-dependent energy release rate during these events.

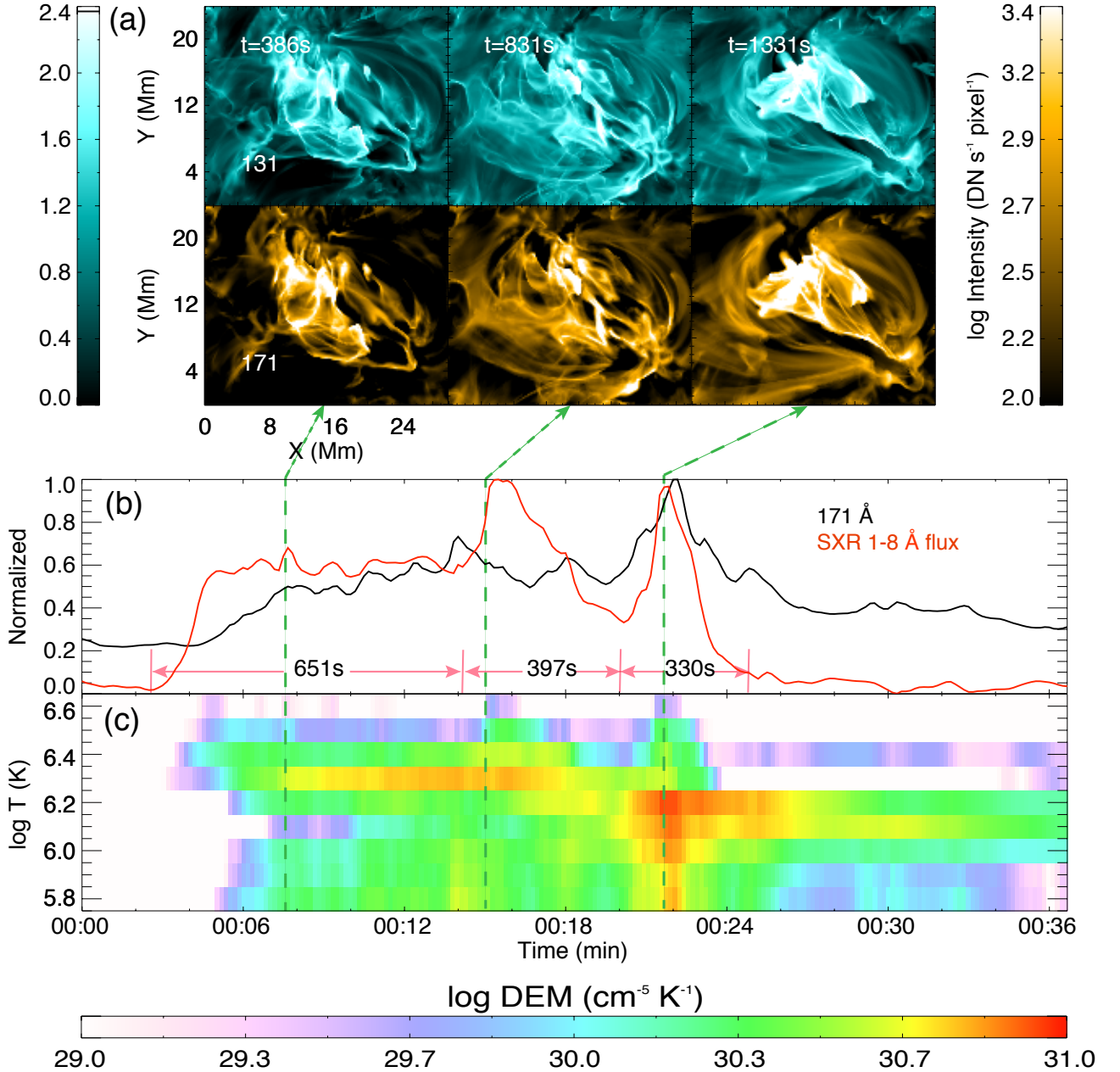


**Figure 2.** Overview of simulated microflares. (a) Snapshots of synthetic 131 Å and 171 Å images at three selected times. (b) Temporal evolution of the SXR 1-8 Å flux (red) and integrated 171 Å intensity (black). Three red line segments indicate three microflares defined by the SXR flux. (c) Temporal evolution of the DEM distribution for the entire region of interest. To address the variations, we subtract the DEM distribution at  $t_0$ . An animation of this figure is available online. The video shows the evolution of three microflares in 131 Å and 171 Å passbands with a duration of 27 s.

The SXR flux of the three microflares reaches a peak of  $10^{-10} \text{ W m}^{-2}$ , two orders smaller than an A-class flare (Figure 2b). On the basis of the synthetic SXR curve, we define roughly the onset and end times of the three microflares. We find that the first microflare has a long duration of about 651 s and

the released magnetic energy is  $10^{27}$ – $10^{28}$  erg. The interesting thing is that the SXR flux seems not to decay after reaching the maximal, with only small fluctuations until the second microflare starts. The second and third microflares are very similar to each other, both presenting an impulsive phase followed by a decay phase, which is consistent with the general evolution pattern for major flares. Their durations are 397 s and 330 s, respectively, and the corresponding magnetic energy release is  $10^{27}$  erg, which is basically in the microflare range. For all events, the total thermal energies are  $10^{28}$ – $10^{29}$  erg, consistent with the estimation of microflares recently observed in [Saqri et al. \(2022\)](#). However, they also found some non-thermal emission during microflares, which is unrealizable in our MHD simulation.

In order to compare with the SXR 1-8 Å flux, we further calculate the EUV intensities of the microflares at different AIA passbands, which are derived through integrating the entire coronal domain. Figure 2b only shows the result for the AIA 171 Å passband. It is clear to see that, for the first and the third microflare, the evolution of the integrated AIA 171 Å intensity resembles that of the SXR flux. However, for the second one, the variation trend of the 171 Å intensity in time is opposite to that of the SXR flux; the rise (decay) phase of the SXR flux approximately corresponds to the decay (rise) phase of the 171 Å intensity. This is mainly due to the different microflare has distinct temperature structures and evolution patterns, which are further revealed by the evolution of their DEM (Figure 2c). For the first microflare, the DEMs at different temperature bins all present a gradual increase, in particular for the warm plasma in the temperature range of  $5.8 \leq \log T \leq 6.2$ . It causes that the enhancement of the 171 Å intensity is more gradual than that of the SXR flux, similar to the events observed by [Saqri et al. \(2022\)](#). For the second microflare, the primary emission is contributed by the hot plasma in the temperature range of  $6.3 \leq \log T \leq 6.5$ ; while, for the plasma in the temperature range of  $5.8 \leq \log T \leq 6.2$ , the DEM does decrease, thus giving rise to the decrease of the 171 Å intensity. For the third microflare, the DEM at all temperatures presents an impulsive increase and then a slow decrease, in good agreement with the evolution of the AIA 171 Å intensity and SXR flux.

### 3.2. 3D Magnetic and Thermodynamic Structures

To disclose how these microflares are generated and how associated plasma is heated, we analyze the three-dimensional magnetic structures of their source region near the peak times. Figures 3a displays the vertical magnetic field distribution at the photosphere with an average strength of 200 Gauss at the base of the first microflare. This value is similar to the strength of the magnetic field at network boundaries (e.g., [Bellot Rubio & Orozco Suárez 2019](#)). It also shows that the microflare is located above a mixed-polarity region that consists of two concentrated polarities. The microflare occurs in the region where a small negative polarity is approaching the major positive polarity. To locate the energy release of the microflare, we overplot the locations of the strong heating rate per particle, which includes the resistive and viscous terms. It is found that the heated plasma is almost co-spatial with the region where the heating rate per particle is maximal (purple isosurface in Figure 3a). We then trace the magnetic field lines from the regions of high heating rate (Figure 3a-c). It is found that the magnetic configuration of the first microflare primarily consists of two groups of highly sheared arcades. The reconnection most likely takes place at the cross point of them. The heated regions present a curved morphology, indicating that the reconnection site is actually a 3D structure. At the same time, the plasma near the reconnection site is heated and then gives rise to the X-ray and EUV emissions we observed.

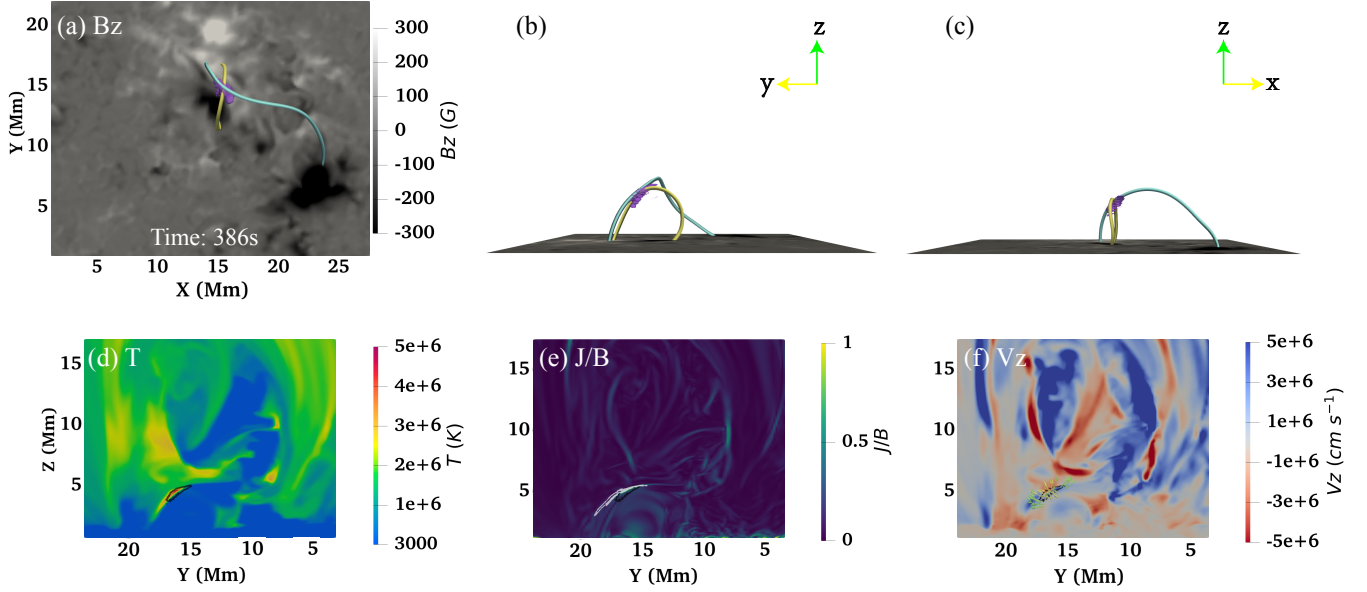


**Figure 3.** 3D magnetic structure and reconnection characteristics near the peak time of the first gradual microflare. (a) Photospheric magnetogram overplotted with reconnecting field lines (yellow and blue). The region with a high heating rate is indicated by transparent purple. (b) and (c) Same as (a) but for different perspectives. (d) Temperature distribution in the  $z$ - $y$  plane crossing the high heating rate region. The contour in black denotes a high heating rate at a level of  $0.5 \text{ erg cm}^{-3} \text{ s}^{-1}$ . (e) Distribution of current density normalized by magnetic field  $J/B$  in the same  $z$ - $y$  plane. The white contour represents the  $\log Q$  of 1.5. (f) Vertical velocity in the same  $z$ - $y$  plane with arrows showing 3D flow field near the reconnection region. The arrows in green (yellow) indicate the outflows (inflows). An animation for the evolution of the temperature and current distributions is available online. The animation proceeds from 386 s to 530 s. The video duration is 2 s.

Interestingly, we find that the reconnection takes place in the chromospheric environment. Figure 3d shows the temperature distribution at the  $z$ - $y$  plane passing the reconnection region. It clearly shows that the temperature around the reconnection region is highly inhomogeneous and the heating mainly occurs at a height of  $4\sim 5 \text{ Mm}$ , where the plasma is heated up to above 1 MK, almost two orders of magnitude higher than the temperature of the surrounding cool plasma of 10 kK. The process was also found to occur in UV bursts, however, the corresponding temperature and energy are smaller than that for microflares studied here (Hansteen et al. 2017). It is also found that the density of the reconnection region ( $\sim 10^{11} \text{ cm}^{-3}$ ), and the energy release rate is estimated to be approximately  $0.5 \text{ erg cm}^{-3} \text{ s}^{-1}$  with a peak value of  $5 \text{ erg cm}^{-3} \text{ s}^{-1}$ , which is enough to heat the local chromospheric plasma to coronal temperature. This value is even comparable to the heating rate required for major flares (Qiu et al. 2012; Liu et al. 2013), implying that major flares may be composed of plentiful microflares. It needs to be mentioned that the chromosphere in the simulation is treated by assuming local thermal equilibrium, the plasma is thus easier to be heated to a higher temperature (Nóbrega-Siverio et al. 2020).

The high heating rate is almost cospatial with the strong current, as seen in the current density distribution of the same  $z$ - $y$  plane (Figure 3e). The squashing factor  $Q$ , which quantitatively describes the degree of change in the connectivity of the field lines (Priest & Démoulin 1995; Titov et al. 2002)



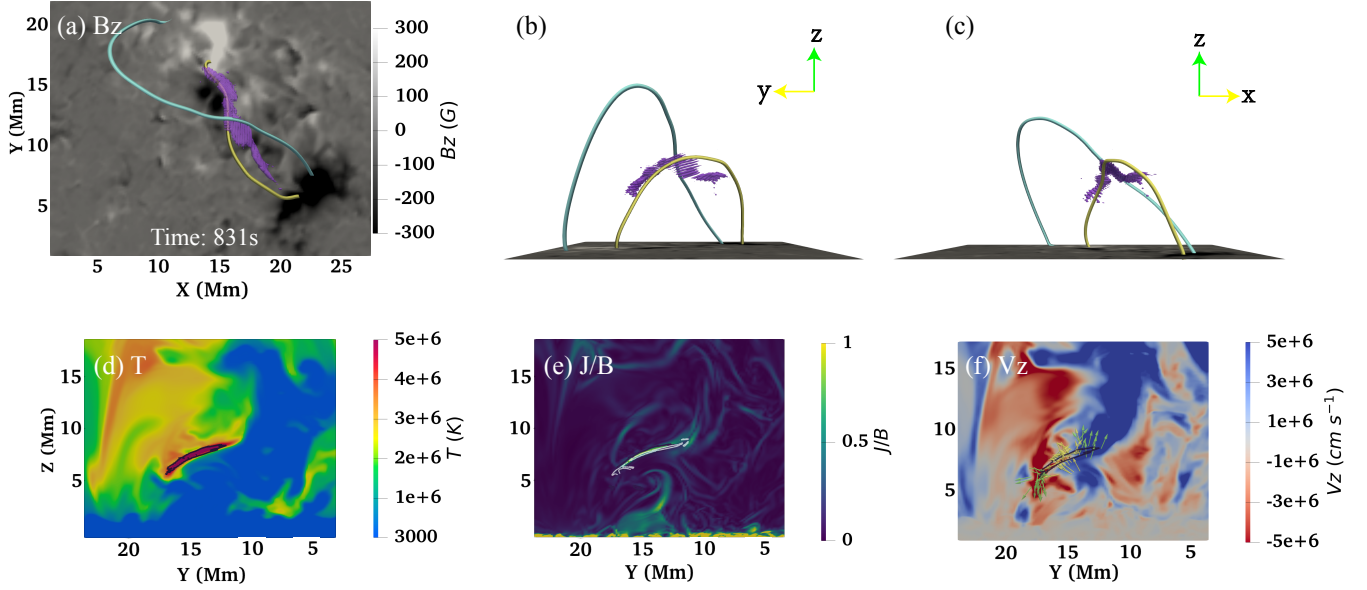


**Figure 4.** Same as Figure 3 but for the second impulsive microflare. An animation for the evolution of the temperature and current distributions is available online. The animation proceeds from 779 s to 1176 s. The video duration is 4 s.

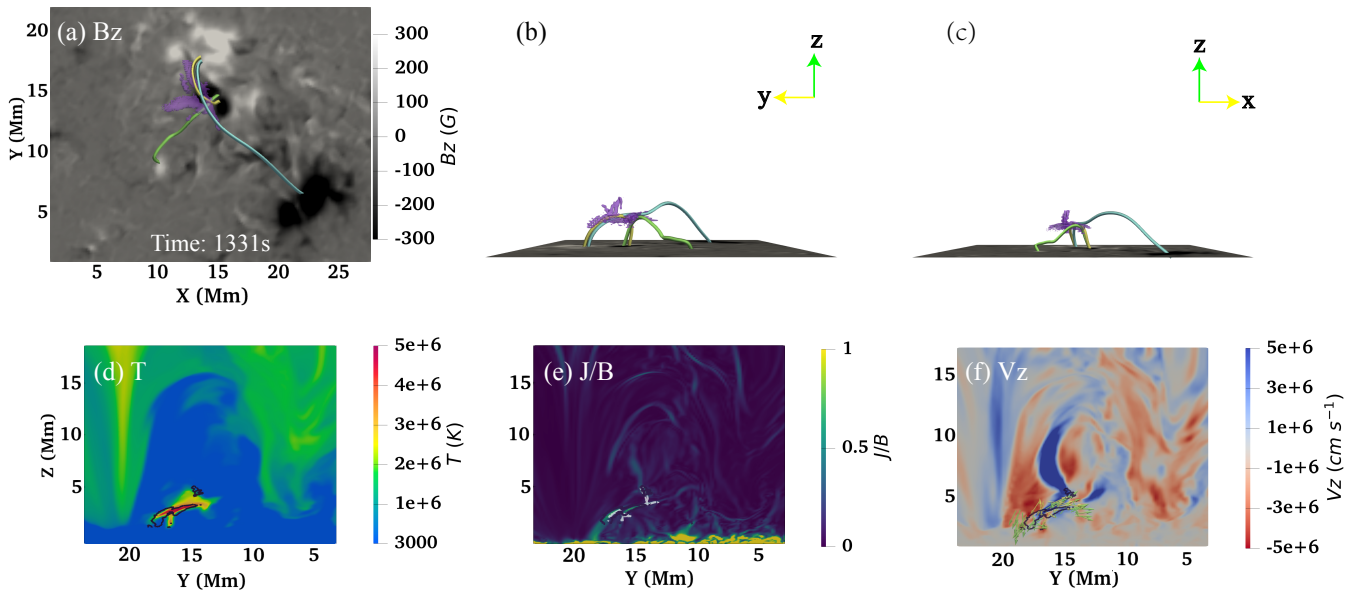


**Figure 5.** Same as Figure 3 but for the third impulsive microflare. **In panel (a), three sets of reconnecting arcades are distinguished with different colors (yellow, blue and green).** An animation for the evolution of the temperature and current distributions is available online. The animation proceeds from 1176 s to 1506 s. The video duration is 3 s.

and is calculated through the method developed by Liu et al. (2016), is shown by the contours in white. It discloses that the reconnection region has the largest  $Q$  values. This is in good agreement



with the argument that magnetic reconnection is prone to occur in the regions where the magnetic field connectivity changes dramatically and the current density maximizes.

During the reconnection, both reconnection inflows and outflows are observed as displayed by the vertical velocity field at the z-y plane and 3D velocity field around the reconnection region (Figure 3f). The velocities of converging inflows are about  $\pm(30\text{--}50)$  km s<sup>-1</sup>. The velocities of outflows are found to be of nearly 100 km s<sup>-1</sup>. These speeds are comparable with that of reconnection outflows revealed both in observations (Peter et al. 2014; Hong et al. 2016) and simulations (Ding et al. 2010) in the chromosphere. Note that the velocity for upward outflows is larger than that for downward outflows (Figure 3f), similar to what was found in a simulation of UV bursts (e.g., Hansteen et al. 2019). Taking the Alfvén speed at the boundaries of the inflows, the reconnection rate is estimated to be  $0.01 \sim 0.1$ . We also inspect the plasma beta  $\beta$ , i.e., the ratio of thermal to magnetic pressure, around the reconnection region and find that it is mostly less than 1 (see Table 1), ranging from 0.001 to 0.01. This shows a high similarity to the reconnection process in the corona as often observed during the CME/flare eruption (Lin 2011; Li et al. 2017).

Because of the long duration of the first microflare, we further inspect the temporal evolution of the 3D magnetic configuration and find that the first microflare primarily consists of three reconnection episodes whose locations are very close to each other. They last for 258 s, 144 s, and 249 s, respectively. The peak of the first microflare actually corresponds to the second reconnection episode. Supplementary Figures S1 and S2 show the 3D magnetic field and thermodynamic properties for the first and third episode. One can see that the magnetic field configuration of the reconnection also appears as a tether-cutting type, very similar to that for the second episode. However, the temperature structure seems to change obviously although the reconnection regions are still located in the chromospheric environment. The basic properties of the reconnection regions for the three episodes are summarized in Table 1.

Figure 4 shows the 3D magnetic structures and reconnection characteristics for the second microflare. Similar to the first long-duration microflare, the reconnection takes place between two sets of highly sheared arcades but with one set of arcades much longer than the other. The reconnection region also has large current densities and Q values (Figure 4e), as well as surrounded by simultaneous inflows and outflows (Figure 4f). While, the difference is that the corresponding reconnection site is located higher, at 5–10 Mm. The plasma density here is about  $10^{10}$  cm<sup>-3</sup>, indicating the environment of the transition region. This could be the reason why the plasma for the second microflare is heated to a higher temperature (almost 5 MK; Figure 4d). **Moreover, only one reconnection episode occurs during this microflare and effectively heats the plasma. The reconnection region is long elongated (Figure 4a-c) and the magnetic configuration does not vary significantly with time.**

For the third impulsive microflare, it is also caused by **one reconnection episode** within an elongated current sheet. Similar to the first event, the reconnection takes place in the chromospheric environment but its height (2–3 Mm) is lower than the first two microflares. **It seems that much energy is released during this event, resulting in the chromospheric plasma near the reconnection region being significantly heated to more than 4 MK.** Note that there are abundant cool plasmas (10 kK) above the reconnection region, thus a fraction of the emission may be absorbed and become invisible. However, the absorption process is not considered when synthesizing EUV images. The morphologies of the high current density and Q values (Figure 5e) highly resemble

**Table 1. Properties of the reconnection during three microflares.**

		Duration (s)	Height (Mm)	Size (Mm)	Temperature (MK) <sup>a</sup>	Plasma $\beta$	Topology	
Event 1 <sup>b</sup>	Episode 1	651	258	5	6	2.5	0.002	Tether-cutting
	Episode 2		144	4 ~ 5	2.5	2	0.006	Tether-cutting
	Episode 3		249	5	3.6	2	0.002	Tether-cutting
Event 2		397	5 ~ 10	11	2	0.004	Tether-cutting	
Event 3		330	2 ~ 3	4	1.6	0.01	Fan-spine-like	

NOTE—<sup>a</sup> Temperature at the DEM peak.

NOTE—<sup>b</sup> The peak of Event 1 corresponds to Episode 2.

that of heated plasma (Figure 5d). The reconnection inflows are mainly contributed by a pair of sheared flows at both sides of the current sheet (Figure 5f). Nevertheless, the 3D structure of the reconnection region is quite different from that for the first and second microflare. As shown in Figure 5a-c, it is more like a 3D fan-spine topology, where three groups of field lines rooted in different polarities concentrate toward the reconnection region, **and persists throughout the event.**

#### 4. SUMMARY AND DISCUSSIONS

In this Letter, we explore the 3D magnetic structures and thermodynamics of three microflares using RMHD simulation data of a solar quiescent region. The main results are summarized as follows.

1. The microflares are produced by magnetic reconnection that occurs at the regions where the current density and Q values are extremely high, and the reconnection properties are summarized in Table 1.

2. The reconnection tends to occur in the lower solar atmosphere where the localized plasma is heated from 10 kK to the coronal temperature above 1 MK and then generates EUV emission. For the second microflare, the released energy is even transported to and thus heats the upper corona.

3. The reconnection region appears as a 3D structure, most likely the quasi-separator near the legs of magnetic loops, varying from tether-cutting to fan-spine-like structure for different events.

The energy release mechanism of the three simulated microflares is similar to that for major flares. In the standard CME/flare model, the magnetic energy is believed to be efficiently released through magnetic reconnection, where the current density and Q values are large (e.g., Sui & Holman 2003; Li et al. 2021). Moreover, the reconnection can drive two oppositely directed outflows along the orientation roughly perpendicular to the converging inflows. These features are all observed during the current three microflares. However, there exists a major difference between the large and small-scaled flares, i.e., whether a CME eruption is involved or not. On the one hand, because of no CME eruption, only a small amount of sheared arcades reconnect, thus leading to microflares being short-lived. It is different from the positive feedback process during the CME/flare eruption, in which a number of arcades are involved in the reconnection process. The reconnection accelerates the CME eruption, which in turn further strengthens the reconnection, thus producing a long-duration flare (e.g., Lin & Forbes 2000; Vršnak 2016; Veronig et al. 2018). On the other hand, during the CME/flare eruption, the reconnection configuration will evolve from a hyperbolic flux tube (HFT) to a vertically stretched sheet-like structure (Cheng et al. 2018). But, during microflares, the reconnection

configuration seems not to be deformed significantly during one event and only likely changes from case to case.

Due to the high-resolution simulated data, the first long-duration microflare is found to be composed of three impulsive reconnection episodes. They share very similar magnetic configurations and thermodynamics, even essentially similar to the following two microflares. Nevertheless, since the three episodes in the first microflare occur continuously in close locations, they are hard to be distinguished, in particular, from the evolution of time-integrated observables such as the SXR 1-8 Å flux.

The 3D magnetic and thermodynamic structures of the microflares revealed here shed some lights on understanding the origin of campfires observed by Solar Orbiter. Recently, [Chen et al. \(2021b\)](#) run a 3D RMHD model for campfires and proposed that they are likely caused by component magnetic reconnection. In their study, the 3D magnetic field structures of the component reconnection are very similar to the tether-cutting type in our study. Observationally, such tether-cutting-like structure was also confirmed to interpret other small-scale transient brightenings similar to campfires (e.g., [Chitta et al. 2021](#); [Mandal et al. 2021](#)). Moreover, we also estimate the heights of the microflares, which range from 2 Mm to 10 Mm above the photosphere, similar to that for campfires ([Berghmans et al. 2021](#)). However, all previous studies believed that campfires were generated in the corona, rather than in the lower atmosphere as we disclose. Furthermore, [Berghmans et al. \(2021\)](#) pointed out that the reconnection responsible for campfires appear at the apexes of intersected loops; nevertheless, our results show that it more likely occurs at the legs of loops. **Very recently, [Tiwari et al. \(2022\)](#) even found some very tiny dot-like EUV brightenings, part of which were identified to be caused by reconnection at a lower height.** In short, we support the argument that, despite a shorter duration, the campfires belong to the flares family and that the corresponding scale resides between microflares and nanoflares.

It is worth mentioning that the magnetic configuration of the microflares is not always the tether-cutting type. Our results show that it may change to a fan-spine-like structure during the third microflare. In fact, such a fan-spine configuration was also observed in smaller-scale (E)UV bursts ([Chitta et al. 2017](#)). Generally speaking, the reconnection tends to occur at null point ([Priest & Pontin 2009](#)), separator ([Longcope et al. 2005](#); [Parnell et al. 2010](#)) or quasi-separator ([Aulanier et al. 2005](#)), where the magnetic connectivity changes drastically. After carefully inspecting the magnetic topology of the three microflares, we do not find any signatures of null point and separator. We thus suggest that the quasi-separator reconnection, appearing as tether-cutting (as shown in [Sun et al. 2015](#)) or fan-spine-like type, could be more common for small-scale events, at least for the microflares we study. No matter which configuration, it is not always the inverse Y-shaped configuration formed by the reconnection between emerging flux and oblique open flux in the microflare models of [Shibata et al. \(1992\)](#) and [Moore et al. \(2010\)](#).

## ACKNOWLEDGMENTS

We thank the referee who raised valuable comments to improve the manuscript. We also thank Hardi Peter, Pradeep Chitta, and Jie Hong for their helpful discussions. AIA data are courtesy of NASA/SDO, which is a mission of NASA's Living With a Star Program. Solar Orbiter is a mission of international cooperation between ESA and NASA, operated by ESA. The EUVI instrument was built by CSL, IAS, MPS, MSSL/UCL, PMOD/WRC, ROB, LCF/IO with funding from the Belgian Federal Science Policy Office (BELSPO/PRODEX PEA 4000112292); the Centre National d'Etudes Spatiales (CNES); the UK Space Agency (UKSA); the Bundesministerium für Wirtschaft und Energie (BMWi) through the Deutsches Zentrum für Luft- und Raumfahrt (DLR); and the Swiss Space Office (SSO). Z.F.L., X.C., and M.D.D. are funded by NSFC grants 11722325, 11733003, 11790303, 11790300, and by National Key R&D Program of China under grant 2021YFA1600504. F.C. is funded by the Fundamental Research Funds for the Central Universities under grant 0201-14380041. Part of the work is supported by the National Center for Atmospheric Research, which is a major facility sponsored by the National Science Foundation under Cooperative Agreement No. 1852977. The high-performance computing support is provided by Cheyenne (doi:10.5065/D6RX99HX).

## REFERENCES

- Archontis, V., & Hansteen, V. 2014, *The Astrophysical Journal*, 788, L2, doi: [10.1088/2041-8205/788/1/L2](https://doi.org/10.1088/2041-8205/788/1/L2)
- Aschwanden, M. J., & Parnell, C. E. 2002, *ApJ*, 572, 1048, doi: [10.1086/340385](https://doi.org/10.1086/340385)
- Aulanier, G., Pariat, E., & Démoulin, P. 2005, *A&A*, 444, 961, doi: [10.1051/0004-6361:20053600](https://doi.org/10.1051/0004-6361:20053600)
- Bellot Rubio, L., & Orozco Suárez, D. 2019, *Living Reviews in Solar Physics*, 16, 1, doi: [10.1007/s41116-018-0017-1](https://doi.org/10.1007/s41116-018-0017-1)
- Berghmans, D., Auchère, F., Long, D. M., et al. 2021, arXiv e-prints, arXiv:2104.03382. <https://arxiv.org/abs/2104.03382>
- Carmichael, H. 1964, *A Process for Flares*, Vol. 50, 451
- Chen, F., Rempel, M., & Fan, Y. 2021a, arXiv e-prints, arXiv:2106.14055. <https://arxiv.org/abs/2106.14055>
- Chen, Y., Przybylski, D., Peter, H., et al. 2021b, arXiv e-prints, arXiv:2104.10940. <https://arxiv.org/abs/2104.10940>
- Cheng, X., Li, Y., Wan, L. F., et al. 2018, *The Astrophysical Journal*, 866, 64, doi: [10.3847/1538-4357/aadd16](https://doi.org/10.3847/1538-4357/aadd16)
- Cheng, X., Zhang, J., Kliem, B., et al. 2020, *The Astrophysical Journal*, 894, 85, doi: [10.3847/1538-4357/ab886a](https://doi.org/10.3847/1538-4357/ab886a)
- Chitta, L. P., Peter, H., Young, P. R., & Huang, Y. M. 2017, *A&A*, 605, A49, doi: [10.1051/0004-6361/201730830](https://doi.org/10.1051/0004-6361/201730830)
- Chitta, L. P., Solanki, S. K., Peter, H., et al. 2021, *A&A*, 656, L13, doi: [10.1051/0004-6361/202141683](https://doi.org/10.1051/0004-6361/202141683)
- Ding, J. Y., Madjarska, M. S., Doyle, J. G., & Lu, Q. M. 2010, *A&A*, 510, A111, doi: [10.1051/0004-6361/200913101](https://doi.org/10.1051/0004-6361/200913101)
- Freeland, S. L., & Handy, B. N. 1998, *Solar Physics*, 182, 497, doi: [10.1023/A:1005038224881](https://doi.org/10.1023/A:1005038224881)
- Glesener, L., Krucker, S., Hannah, I. G., et al. 2017, *ApJ*, 845, 122, doi: [10.3847/1538-4357/aa80e9](https://doi.org/10.3847/1538-4357/aa80e9)
- Graham, D. R., De Pontieu, B., & Testa, P. 2019, *ApJL*, 880, L12, doi: [10.3847/2041-8213/ab2f91](https://doi.org/10.3847/2041-8213/ab2f91)
- Hansteen, V., Ortiz, A., Archontis, V., et al. 2019, *A&A*, 626, A33, doi: [10.1051/0004-6361/201935376](https://doi.org/10.1051/0004-6361/201935376)
- Hansteen, V. H., Archontis, V., Pereira, T. M. D., et al. 2017, *The Astrophysical Journal*, 839, 22, doi: [10.3847/1538-4357/aa6844](https://doi.org/10.3847/1538-4357/aa6844)
- Hirayama, T. 1974, *SoPh*, 34, 323, doi: [10.1007/BF00153671](https://doi.org/10.1007/BF00153671)
- Hong, J., Ding, M. D., Li, Y., et al. 2016, *ApJL*, 820, L17, doi: [10.3847/2041-8205/820/1/L17](https://doi.org/10.3847/2041-8205/820/1/L17)

- Hudson, H. S. 1991, *SoPh*, 133, 357, doi: [10.1007/BF00149894](https://doi.org/10.1007/BF00149894)
- Inglis, A. R., & Christe, S. 2014, *ApJ*, 789, 116, doi: [10.1088/0004-637X/789/2/116](https://doi.org/10.1088/0004-637X/789/2/116)
- Jess, D. B., Mathioudakis, M., Browning, P. K., Crockett, P. J., & Keenan, F. P. 2010, *ApJL*, 712, L111, doi: [10.1088/2041-8205/712/1/L111](https://doi.org/10.1088/2041-8205/712/1/L111)
- Jiang, R. L., Fang, C., & Chen, P. F. 2010, *The Astrophysical Journal*, 710, 1387, doi: [10.1088/0004-637x/710/2/1387](https://doi.org/10.1088/0004-637x/710/2/1387)
- Jiang, R. L., Fang, C., & Chen, P. F. 2012, *ApJ*, 751, 152, doi: [10.1088/0004-637X/751/2/152](https://doi.org/10.1088/0004-637X/751/2/152)
- Kopp, R. A., & Pneuman, G. W. 1976, *SoPh*, 50, 85, doi: [10.1007/BF00206193](https://doi.org/10.1007/BF00206193)
- Krucker, S., Hurford, G. J., Grimm, O., et al. 2020, *A&A*, 642, A15, doi: [10.1051/0004-6361/201937362](https://doi.org/10.1051/0004-6361/201937362)
- Kuhar, M., Krucker, S., Glesener, L., et al. 2018, *The Astrophysical Journal*, 856, L32, doi: [10.3847/2041-8213/aab889](https://doi.org/10.3847/2041-8213/aab889)
- Lemen, J. R., Title, A. M., Akin, D. J., et al. 2012, *SoPh*, 275, 17, doi: [10.1007/s11207-011-9776-8](https://doi.org/10.1007/s11207-011-9776-8)
- Li, T., Priest, E., & Guo, R. 2021, *Proceedings of the Royal Society of London Series A*, 477, 20200949, doi: [10.1098/rspa.2020.0949](https://doi.org/10.1098/rspa.2020.0949)
- Li, X., Guo, F., Li, H., & Li, G. 2017, *ApJ*, 843, 21, doi: [10.3847/1538-4357/aa745e](https://doi.org/10.3847/1538-4357/aa745e)
- Lin, J., & Forbes, T. G. 2000, *J. Geophys. Res.*, 105, 2375, doi: [10.1029/1999JA900477](https://doi.org/10.1029/1999JA900477)
- Lin, R. P. 2011, *SSRv*, 159, 421, doi: [10.1007/s11214-011-9801-0](https://doi.org/10.1007/s11214-011-9801-0)
- Liu, R., Kliem, B., Titov, V. S., et al. 2016, *ApJ*, 818, 148, doi: [10.3847/0004-637X/818/2/148](https://doi.org/10.3847/0004-637X/818/2/148)
- Liu, W.-J., Qiu, J., Longcope, D. W., & Caspi, A. 2013, *The Astrophysical Journal*, 770, 111, doi: [10.1088/0004-637x/770/2/111](https://doi.org/10.1088/0004-637x/770/2/111)
- Longcope, D. W., McKenzie, D. E., Cirtain, J., & Scott, J. 2005, *ApJ*, 630, 596, doi: [10.1086/432039](https://doi.org/10.1086/432039)
- Mandal, S., Peter, H., Pradeep Chitta, L., et al. 2021, arXiv e-prints, arXiv:2111.08106. <https://arxiv.org/abs/2111.08106>
- Moore, R. L., Cirtain, J. W., Sterling, A. C., & Falconer, D. A. 2010, *The Astrophysical Journal*, 720, 757, doi: [10.1088/0004-637x/720/1/757](https://doi.org/10.1088/0004-637x/720/1/757)
- Müller, D., St. Cyr, O. C., Zouganelis, I., et al. 2020, *A&A*, 642, A1, doi: [10.1051/0004-6361/202038467](https://doi.org/10.1051/0004-6361/202038467)
- Ning, Z. 2008, *The Astrophysical Journal*, 686, 674, doi: [10.1086/590652](https://doi.org/10.1086/590652)
- Nóbrega-Siverio, D., Moreno-Insertis, F., Martínez-Sykora, J., Carlsson, M., & Szydlarski, M. 2020, *A&A*, 633, A66, doi: [10.1051/0004-6361/201936944](https://doi.org/10.1051/0004-6361/201936944)
- Parnell, C. E., Haynes, A. L., & Galsgaard, K. 2010, *Journal of Geophysical Research (Space Physics)*, 115, A02102, doi: [10.1029/2009JA014557](https://doi.org/10.1029/2009JA014557)
- Peter, H., Tian, H., Curdt, W., et al. 2014, *Science*, 346, 1255726, doi: [10.1126/science.1255726](https://doi.org/10.1126/science.1255726)
- Priest, E. R., & Démoulin, P. 1995, *J. Geophys. Res.*, 100, 23443, doi: [10.1029/95JA02740](https://doi.org/10.1029/95JA02740)
- Priest, E. R., & Pontin, D. I. 2009, *Physics of Plasmas*, 16, 122101, doi: [10.1063/1.3257901](https://doi.org/10.1063/1.3257901)
- Qiu, J., Liu, C., Gary, D. E., Nita, G. M., & Wang, H. 2004, *The Astrophysical Journal*, 612, 530, doi: [10.1086/422401](https://doi.org/10.1086/422401)
- Qiu, J., Liu, W.-J., & Longcope, D. W. 2012, *ApJ*, 752, 124, doi: [10.1088/0004-637X/752/2/124](https://doi.org/10.1088/0004-637X/752/2/124)
- Rempel, M. 2017, *ApJ*, 834, 10, doi: [10.3847/1538-4357/834/1/10](https://doi.org/10.3847/1538-4357/834/1/10)
- Rochus, P., Auchère, F., Berghmans, D., et al. 2020, *A&A*, 642, A8, doi: [10.1051/0004-6361/201936663](https://doi.org/10.1051/0004-6361/201936663)
- Saqri, J., Veronig, A. M., Warmuth, A., et al. 2022, arXiv e-prints, arXiv:2201.00712. <https://arxiv.org/abs/2201.00712>
- Shibata, K., Ishido, Y., Acton, L. W., et al. 1992, *PASJ*, 44, L173
- Sturrock, P. A. 1966, *Nature*, 211, 695, doi: [10.1038/211695a0](https://doi.org/10.1038/211695a0)
- Sui, L., & Holman, G. D. 2003, *The Astrophysical Journal*, 596, L251, doi: [10.1086/379343](https://doi.org/10.1086/379343)
- Sun, J. Q., Cheng, X., Ding, M. D., et al. 2015, *Nature Communications*, 6, 7598, doi: [10.1038/ncomms8598](https://doi.org/10.1038/ncomms8598)
- Testa, P., Polito, V., & Pontieu, B. D. 2020, *The Astrophysical Journal*, 889, 124, doi: [10.3847/1538-4357/ab63cf](https://doi.org/10.3847/1538-4357/ab63cf)
- Titov, V. S., Hornig, G., & Démoulin, P. 2002, *Journal of Geophysical Research (Space Physics)*, 107, 1164, doi: [10.1029/2001JA000278](https://doi.org/10.1029/2001JA000278)
- Tiwari, S. K., Hansteen, V. H., De Pontieu, B., et al. 2022, arXiv:2203.06161



- Veronig, A. M., Podladchikova, T., Dissauer, K., et al. 2018, *ApJ*, 868, 107, doi: [10.3847/1538-4357/aaeac5](https://doi.org/10.3847/1538-4357/aaeac5)
- Vögler, A., Shelyag, S., Schüssler, M., et al. 2005, *A&A*, 429, 335, doi: [10.1051/0004-6361:20041507](https://doi.org/10.1051/0004-6361:20041507)
- Vršnak, B. 2016, *Astronomische Nachrichten*, 337, 1002, doi: [10.1002/asna.201612424](https://doi.org/10.1002/asna.201612424)
- Yashiro, S., Gopalswamy, N., Akiyama, S., Michalek, G., & Howard, R. A. 2005, *Journal of Geophysical Research (Space Physics)*, 110, A12S05, doi: [10.1029/2005JA011151](https://doi.org/10.1029/2005JA011151)
- Zhang, J., Dere, K. P., Howard, R. A., Kundu, M. R., & White, S. M. 2001, *The Astrophysical Journal*, 559, 452, doi: [10.1086/322405](https://doi.org/10.1086/322405)
- Zhang, J., Kundu, M. R., & White, S. M. 2001, *SoPh*, 198, 347, doi: [10.1023/A:1005222616375](https://doi.org/10.1023/A:1005222616375)

## 5. APPENDIX

We find that the first microflare is primarily composed of three reconnection episodes. In Sect. 3.2, we only show the second episode that occurs near the peak time of the SXR 1–8 Å flux. Here, we display the other two episodes as shown in Figure S1 and Figure S2. One can see that, for both of them, the reconnection also takes place between two groups of highly sheared arcades. The main difference is that the reconnection region for the first episode is long stretched, rather than localized during the second episode. Moreover, the peak temperature considerably increases compared with the other two.

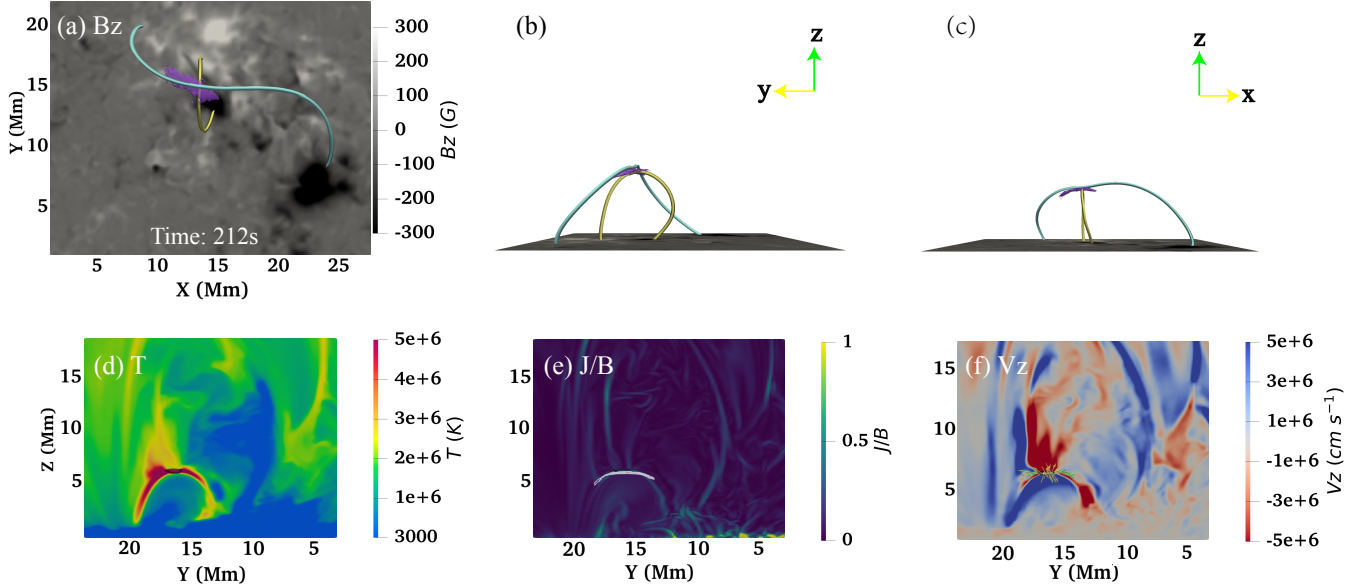


**Figure S1.** Same as Figure 3 but for the first reconnection episode of the first microflare. An animation for the temperature and current distributions is available online. The animation proceeds from 128 s to 386 s. The video duration is 3 s.

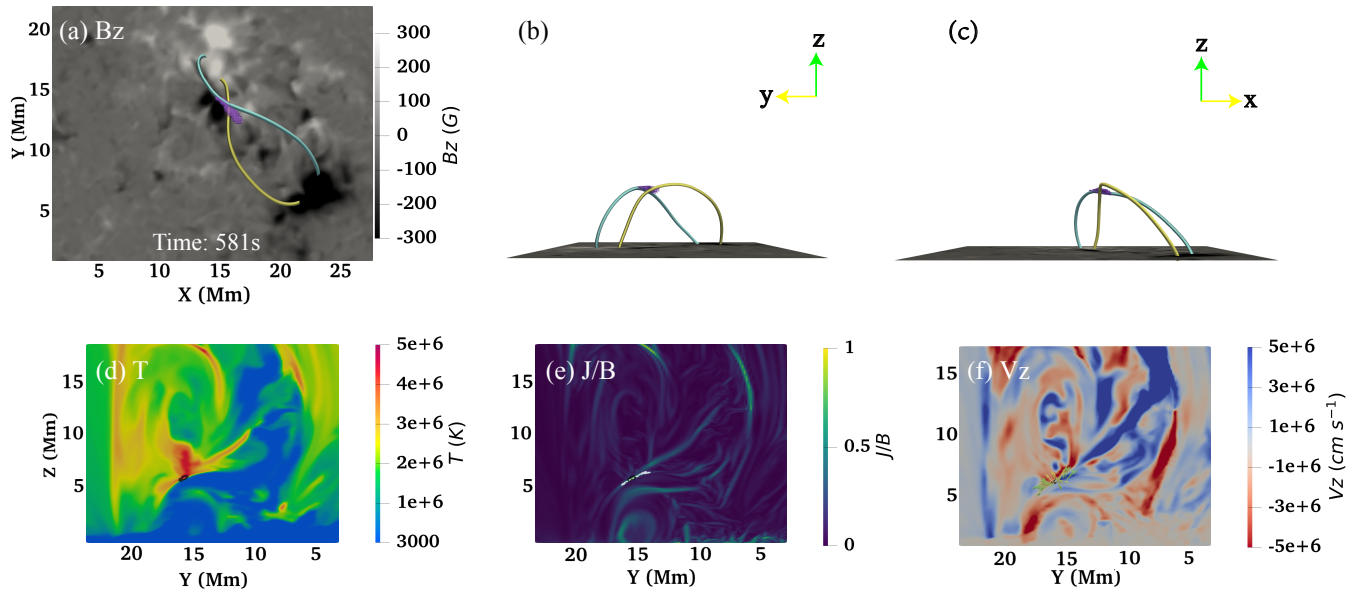


**Figure S2.** Same as Figure 3 but for the third reconnection episode of the first microflare. An animation for the temperature and current distributions is available online. The animation proceeds from 530 s to 779 s. The video duration is 3 s.